Controlling acoustic non-Hermitian skin effect via synthetic magnetic fields

He Gao,[1] Weiwei Zhu,[2] Haoran Xue,[3, a)] Guancong Ma,[4, b)] and Zhongqing Su[1, c)]

[1)] *Department of Mechanical Engineering, The Hong Kong Polytechnic University, Kowloon, Hong Kong SAR, China*

[2)] *Department of Physics, Ocean University of China, Qingdao, China*

[3)] *Department of Physics, The Chinese University of Hong Kong, Shatin, Hong Kong SAR, China*

[4)] *Department of Physics, Hong Kong Baptist University, Kowloon Tong, Hong Kong, China*

Non-Hermitian skin effect (NHSE) is an intrinsic non-Hermitian phenomenon where an extensive number of eigenmodes, called skin modes, are localized at the boundary of a system. Recent theories have suggested that the NHSE can be well-tuned by external fields, opening a route to manipulating wave localization. Here, we experimentally demonstrate the diverse interactions between NHSE and synthetic magnetic fields (SMFs) in coupled acoustic ring resonator lattices. We observe that the NHSE and SMFs can, via different physical mechanisms, compete or synergize, resulting in either the suppression or the creation of NHSE. With the aid of the complex frequency excitation technique, we experimentally observe that SMFs can suppress the NHSE by introducing Landau quantization, causing localization to move towards the bulk. In contrast, we show that, the presence of SMF generates topological edge modes in the lattice, which then become corner skin modes by the second-order NHSE. Our results evidence the rich physics and diverse consequences that arise from the interplay of magnetic fields and NHSE, paving the way for actively controlling wave localization.

I. INTRODUCTION

Non-Hermitian systems have gained widespread research interest in recent years owing to their rich physics and prospective applications[1–6]. One of the most prominent phenomena in non-Hermitian systems is non-Hermitian skin effect (NHSE), whereby the spectrum under periodic boundary condition (PBC) is characterized by nontrivial point gap topology and enormous boundary-localized eigenstates, known as skin modes, emerging under open boundary condition (OBC)[7–11]. The NHSE results in the failure of the Bloch theory, leading to a breakdown of conventional bulk-boundary correspondence and the dependence of the OBC eigenspectrum to boundary conditions[10–12]. Furthermore, the skin modes can cover a large energy window and are robust against moderate disorder owing to their topological nature[9,13–17], which are appealing properties for classical wave devices as they enable broadband and robust wave localization. So far, the NHSE has been realized in a variety of classical wave platforms including acoustics[18–23], mechanics[24–27], photonics[16,28,29] and topolectrical circuits[30–32], with potential applications in efficient wave funneling[16], mode morphing[26], lasing[33,34] and enhanced sensing[35–37].

A magnetic field applied to a two-dimensional (2D) system can lead to a variety of different phenomena. The emergence of Landau quantization, by which an extensive number of modes become localized in the bulk, is perhaps the most celebrated effect[38]. On the other hand, applying magnetic flux through certain 2D lattices also creates topologically nontrivial states[39], in which localized modes, viz, topological edge states, appear at the boundary of the specimen. The interplay of magnetic fields and non-Hermiticity has been an attractive topic of research. For example, it has been theoretically shown that Landau quantization can suppress the NHSE, due to the competition between the two distinct localization mechanisms[40–43]. Yet in other scenarios, magnetic fields and non-Hermiticity work together to give rise to the second-order NHSE[44], leading to corner skin modes in 2D systems. Consequently, the combination of magnetic field and NHSE can lead

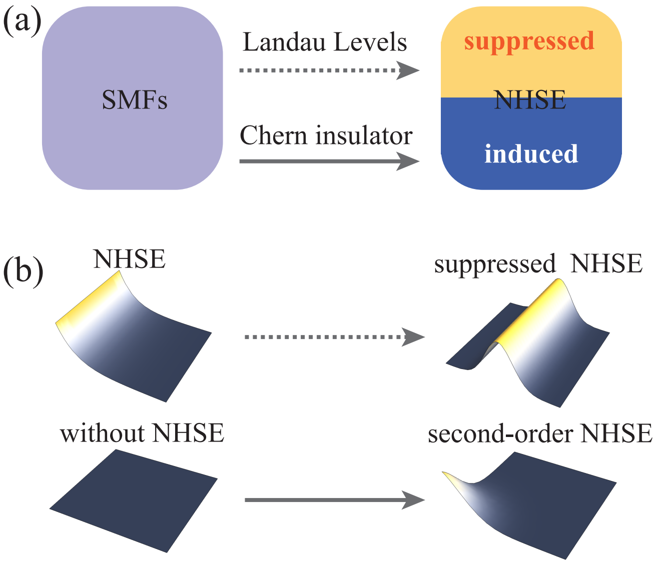

FIG. 1. (a) Schematic of the interaction of NHSE and SMF: the magnetic field induces Landau Levels and Chern insulators, leading to the suppression and generation of NHSE. (b) The SMF can push some of the skin modes to localize in the bulk (upper panel) while creating chiral edge modes that facilitate the second-order NHSE (lower panel).

[a)] Electronic mail: haoranxue@cuhk.edu.hk

[b)] Electronic mail: phgcma@hkbu.edu.hk

[c)] Electronic mail: zhongqing.su@polyu.edu.hk

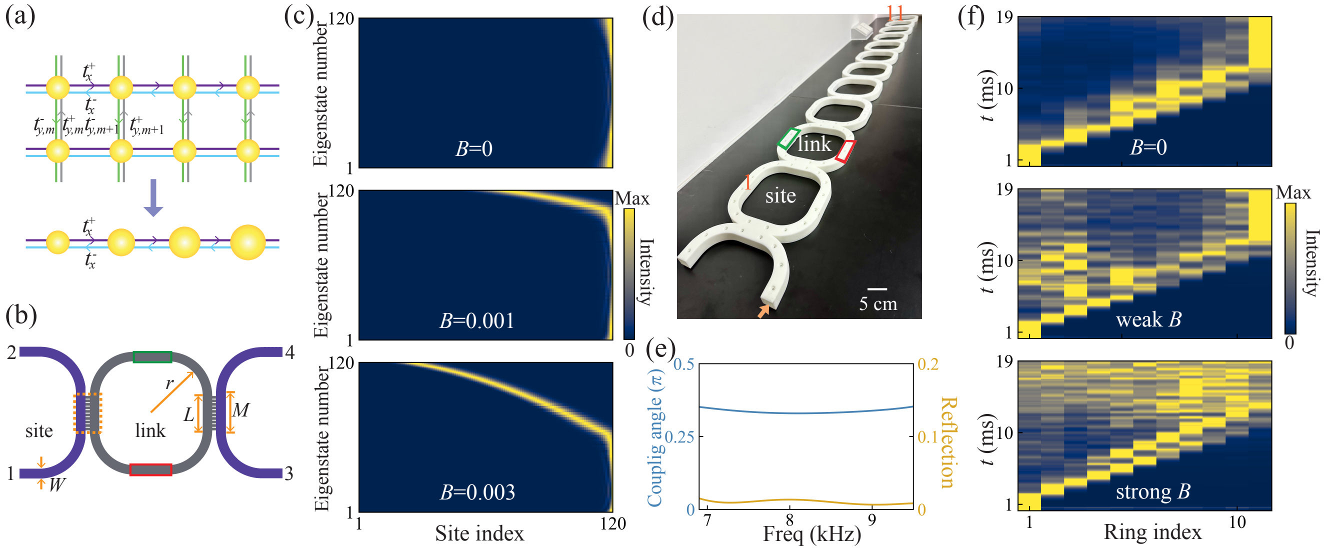

FIG. 2. (a) Illustration of the tight-binding model exhibiting first-order NHSE. (b) Illustration of one unit cell in the coupled ring lattice.(c) Eigenstates of the lattice under x-OBC and y-PBC with different B. The magnetic field $B = 0,\ 0.001,\ 0.003$ (top to bottom panel), respectively. In the calculations, $M = 120,\ N = 1,\ t_0 = 1,\ \delta = 0.4,\ k_y = 0$. (d) Photo of the printed sample without acoustic synthetic magnetic field. (e) Calculated coupling coefficient and reflection as a function of frequency. (f) Measured acoustic intensity profiles with the evolution of time under different synthetic magnetic field strength. In (c) and (f), the intensity profile at each moment is respectively normalized by the peak value at that time.

to diverse consequences [see Fig. 1(a)], which significantly enhances the flexibility of controlling wave localization and opens up new possibilities for a wide range of applications.

In this Letter, we investigate the rich physics and diverse consequences resulting from the interplay between SMFs and NHSE. SMFs are gauge fields appearing as effective magnetic fields in the Hamiltonian. Achievable by artificial designs, such as geometric deformation of the lattice or application of modulation potentials, SMFs do not rely on electromagnetic interactions and, therefore, affect neutral particles, making them suitable for manipulating light and sound[45,46]. Our experimental works are based on non-Hermitian coupled ring acoustic lattices. First, SMFs are introduced to generate Landau levels, which then competitively interact with NHSE, as illustrated in the upper panel of Fig. 1(b). Second, an SMF is used to create a Chern insulator, giving rise to topological edge states which then become corner skin modes by the NHSE, as illustrated in the lower panel of Fig. 1(b). The essential components, including complex and asymmetrical couplings, which allow for the realization of the NHSE, are implemented with engineered loss. A complex frequency excitation technique is used to probe the NHSE in this passive acoustic system[21].

II. SUPPRESSION OF NHSE BY SMFS

We first study the suppression of the first-order NHSE by magnetic fields. Consider a 2D tight-binding model as illustrated in the upper panel of Fig. 2(a). The corresponding Hamiltonian is:

$$H = \sum_{m=1,n=1}^{M,N} (t_x^+ c_{m+1,n}^\dagger c_{m,n} + t_x^- c_{m,n}^\dagger c_{m+1,n} + t_{y,m}^- c_{m,n+1}^\dagger c_{m,n} + t_{y,m}^+ c_{m,n}^\dagger c_{m,n+1}), \tag{1}$$

where $c_{m,n}^\dagger$ ($c_{m,n}$) is the creation (annihilation) operator on site (m,n). M and N denote the number of sites along x and y directions, respectively. The couplings along x direction are asymmetric: $t_x^\pm = t_0 \pm \delta$, leading to the NHSE. The couplings along y direction are complex: $t_{y,m}^\pm = t_0 e^{\pm i2\pi mB}$, yielding the gauge field $\boldsymbol{A} = B(0,x)$ with B denoting the corresponding uniform magnetic field. Noting that the periodicity along y direction is not affected by the magnetic field, we reduce this 2D lattice to a 1D one by fixing $k_y = 0$, which greatly facilitates the implementation. The resulting lattice, as shown in the lower panel of Fig. 2(a), has an on-site modulation $2t_0\cos(2\pi mB + k_y)$ due to the magnetic field. Practically, this 1D model can be realized in a coupled acoustic ring resonator lattice with losses on the link rings and modulated sizes of link rings [Fig. 2(b)].

Figure 2(c) displays the calculated eigenstates (under OBC) of the 1D lattice model for different values of B. When $B = 0$, all OBC eigenstates are localized at the right boundary, which are standard features of NHSE. Upon increasing B, an increasing number of eigenstates are pushed into the bulk, showing that NHSE is suppressed by SMF. We note that similar suppression behavior can also be observed for other k_y (see supplementary material[47]).

The acoustic lattice is a periodic array of ring resonators, as shown in Fig. 2(d). The rings are coupled by periodically arranged small tubes, as indicated by the dashed orange box

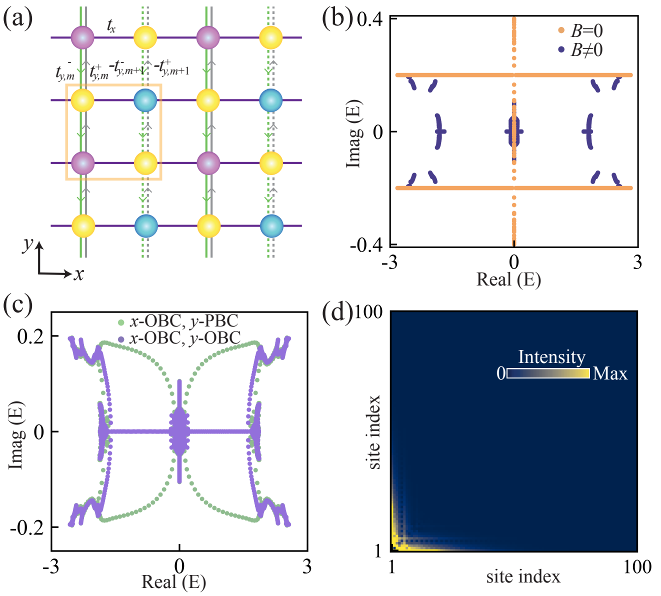

FIG. 3. (a) Schematic illustration of the lattice in Eq. 2. The coupling strengths along x and y directions are t_x and $t^{\pm}_{y,m}$, respectively. The elements in purple and blue have additional loss ($-\gamma$) and gain (γ). (b) Complex spectra for the lattice without (orange dots) and with (blue dots) magnetic field under x-PBC and y-PBC. (c) Complex spectra for the lattice with magnetic field under x-OBC, y-PBC (green dots) and y-OBC (purple dots), respectively. (d) The intensity profile for one skin mode in a finite lattice with magnetic field. In all calculations, $t_x = 1$, $t^{\pm}_{y,m} = (-1)^{m+1} e^{\pm i2\pi mB}$ (m is the column number, B is the strength of the magnetic field) $M = N = 100$, $B = 0.1$, $\gamma = 0.4$ and $k_y = 0$ for y-PBC.

in Fig. 2(b). There are two types of rings, one plays the role of onsite orbitals, denoted as site rings, and the others provide coupling, denoted as link rings. The SMF is implemented by tuning the circumference of the site rings. The reciprocal coupling coefficient t_0 is determined by the small tubes between the site and link rings. The asymmetric coupling $\pm\delta$ are realized by inserting sound-absorptive materials into the region highlighted by the green box on the link rings such that the wave passing through this region is attenuated. We have optimized the coupling area such that the reflection is neglectable (thus we only focus on the modes with clockwise circulation direction in the site rings) [see Fig. 2(e)]. The whole structure is filled with air and surrounded by hard walls. All structural parameters are given in supplementary material[47]. This coupled acoustic ring resonator lattice can be modeled by the transfer matrix method. When the coupling strength in the coupling region is small and the site and link rings are near anti-resonance, the lattice can capture the tight-binding model [47].

Because of the absence of gain, the acoustic lattice is loss-biased and the sound inside attenuates rapidly, which makes it difficult to visualize the skin modes using a constant-intensity source[21]. Recently, a new excitation method, called complex-frequency excitation, was developed to compensate for the loss in such systems[21,48–50]. The complex-frequency excitation pumps the system using an incident signal modulated by a specific amount of temporal decay, which corresponds to the virtual gain effect inside the system. A complex frequency signal of 8240+200i Hz with finite length is launched at the left side of the lattice[47]. When the sound passes through the red (green) region in the link ring, the excitation signal decay is faster (slower) than the decay caused during propagation, leading to an amplification (attenuation) effect[47]. By capturing the time-domain signals at all positions of the whole sample, we experimentally obtain time- and site-resolved results for three samples with different B. As shown in the top panel of Fig. 2(f), the sound wave propagates towards the right and eventually stops at the right edge without any reflection when $t > 15$ms in the lattice without SMFs – a clear indication of the NHSE. However, as B increases, a portion of wave energy stops in the bulk, whereas the rest reaches the right edge [middle panel of Fig. 2(f)]. This indicates that the onset of Landau quantization and B is competing with NHSE. By further increasing B, Landau quantization eventually dominates over NHSE [bottom panel of Fig. 2(f)]. These results clearly demonstrate the suppression of NHSE by magnetic fields.

III. CREATION OF NHSE BY SMFS

Next, we demonstrate that magnetic fields can also induce NHSE. To this end, consider a 2D non-Hermitian lattice model with on-site gain and loss [Fig. 3(a)]:

$$
\begin{aligned}
H = \sum_{m=1,n=1}^{M,N} & \left(t_x c^{\dagger}_{m,n} c_{m+1,n} + t_x c^{\dagger}_{m+1,n} c_{m,n}\right. \\
& + (-1)^{m+1} t^{-}_{y,m} c^{\dagger}_{m,n+1} c_{m,n} + (-1)^{m+1} t^{+}_{y,m} c^{\dagger}_{m,n} c_{m,n+1} \\
& \left. + i\frac{(-1)^m + (-1)^n}{2} \gamma c^{\dagger}_{m,n} c_{m,n}\right).
\end{aligned}
\tag{2}
$$

Each unit cell, as indicated by the orange box in Fig. 3(a), consists of four sites with different on-site gain or loss. The purple (blue) site has loss (gain) of $-i\gamma$ ($i\gamma$), whereas the two yellow sites have no loss or gain.

In the absence of a magnetic field, the spectrum under PBCs in both directions forms straight lines in the complex plane [see the orange dots in Fig. 3(b), more details are provided in the supplementary material], indicating that there is no NHSE[44]. The absence of NHSE is also verified by inspecting the eigenstates under OBCs, as given in supplementary material[47]. Then, we apply an out-of-plane magnetic field B to the lattice by threading a flux 0.2π in each plaquette. This splits the PBC spectrum into multiple sectors, with two large real line gaps emerging [see the blue dots in Fig. 3(b)]. These bandgaps induced by the magnetic fields, are topological and they are closed by chiral edge modes when the system is under x-OBC, y-PBC [see the green dots in Fig. 3(c)]. In the presence of non-Hermiticity, i.e., gain and loss, these chiral edge modes will be attenuated or amplified as they propagate along the boundaries, depending on the non-Hermiticity at the boundary. For an OBC lattice with an even number of sites in both directions, the chiral edge modes on the bottom and right edges will be amplified, whereas those on the top and left

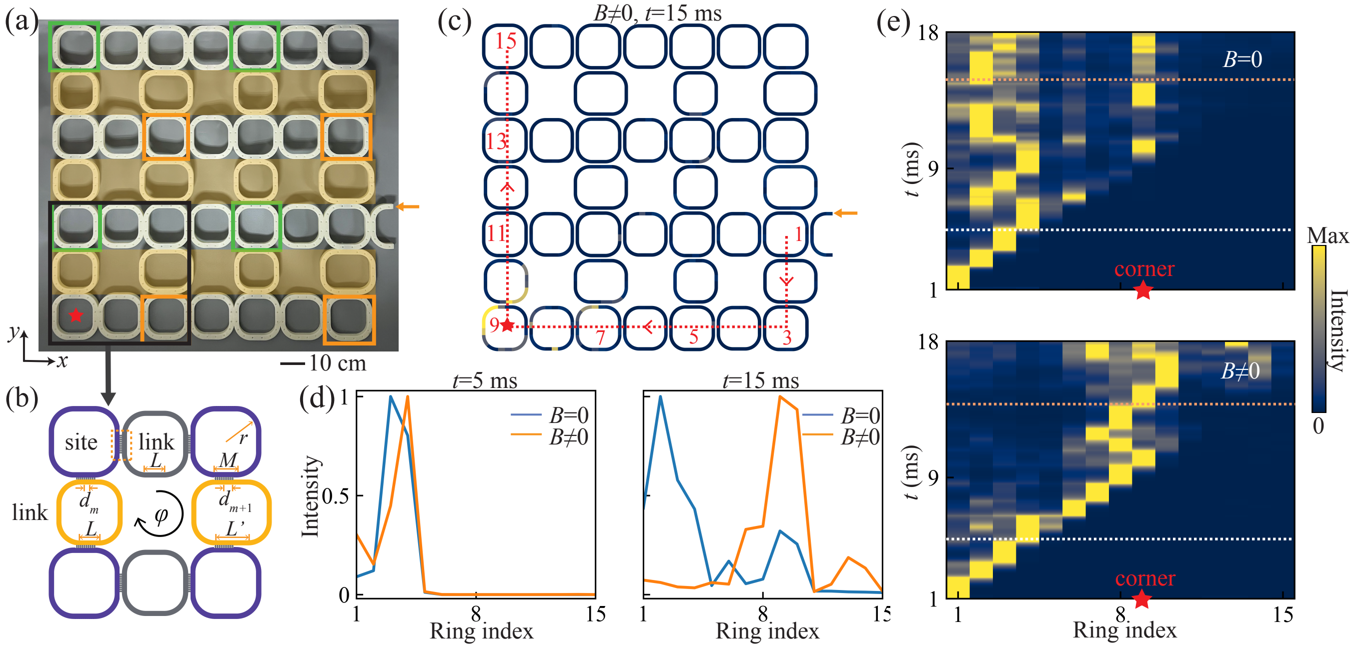

FIG. 4. (a) Photo of the sample without B, which is composed of 4×4 site rings coupled with link rings along x, y directions. The sites in green (orange) boxes have additional loss (no additional loss), while the remaining sites have less additional loss. The half ring on the right side is for inputting excitation signal. (b) Details of one unit cell in (a). The structural parameters M=6 cm, r=5.5 cm, L=5.48 cm, r=5.5 cm, L'=9.72 cm, $d_n = md_0$ (d_0=0.5 cm, m=1,2,3,4) and $\varphi = 0.76\pi$. (c) Measured acoustic energy profiles for the lattice with B at t=15 ms. (d) Measured intensity distributions for the lattice without (blue line) and with (orange line) B along the red dashed line in (a) at t=5 ms and t=15 ms, respectively. (e) Measured intensity profiles as a function of time t for the lattice without (upper panel) and with (lower panel) B. The intensity profile at each moment is respectively normalized by the peak value at that time. The red star marks the corner ring site in (a).

edges will be attenuated. This leads to a second-order NHSE: the edge spectrum under full OBCs lies inside that under x-OBC, y-PBC [Fig. 3(c)] and the corresponding eigenstates are localized at the lower-left corner [Fig. 3(d)]. The skin corner localization can be pushed to the upper-right corner by reversing the direction of the synthetic magnetic field [details see the supplementary material]. In this case, the role of the magnetic field is to induce the NHSE, through nontrivial point-gap topology of edge states in nontrivial line gaps created by the magnetic field.

To realize this phenomenon in the experiment, we design a 2D coupled acoustic ring resonator lattice as shown in Fig. 4(a). The structure, consisting of site rings coupled through link rings, is very similar to the one used in Fig. 2. To realize the required negative couplings, we adjust the sizes of the corresponding link rings such that there is a π phase shift in the coupling[51]. Sound absorptive materials are inserted into the site rings highlighted by the green boxes, while the site rings in orange boxes remain unchanged. Half the amount of sound absorptive materials are inserted into the remaining site rings. Under such a setting, when we launch a sound signal with a complex frequency of 8120+194i Hz with finite length, the sites in the green (orange) boxes will exhibit virtual loss (gain), yielding an effective value of γ being approximately 73 Hz [details are provided in the supplementary material]. For this lattice with $B = 0$, the intensity evolution along the edges [indicated by the red dashed line in Fig. 4(a)] shows a spreading of signal over the edges, without any unidirectional propagation or corner localization [see Fig. 4(e)]. We also measure the intensity field in the whole lattice at t=15 ms, where no corner localization is observed, as demonstrated in supplementary material[47].

We then investigate the dynamics under a nonzero SMF, which is implemented in the lattice rather than using onsite modulations to mimic the effect of a magnetic field at a fixed momentum. To this end, we move the link rings shaded in yellow in Fig. 4(a) towards the right side[52,53]. The moved distance d_m ($d_m = md_0$) for the three link rings in the same column is identical. Here, d_0 is designed to be 0.5 cm, yielding an effective magnetic flux $\varphi = 0.76\pi$ for each plaquette. Interestingly, the measured intensity evolution is quite different from that without B. As shown in the lower panel of Fig. 4(e), the evolution pattern exhibits a clear unidirectional propagation when $t < 10$ ms. At around $t = 10$ ms, the sound signal reaches the lower left corner. After $t > 10$ ms, the sound stops propagation and remains localized at the corner, indicating the corner skin effect. We also plot the intensity distribution in the whole lattice at t=15 ms, as presented in Fig. 4(c), which clearly shows that the sound power is highly localized at the lower-left corner. Figure 4(d) compares the intensity profiles along the boundaries without and with B at t=5 ms [dashed white line in Fig. 4(e)] and t=15 ms [dashed orange line in Fig. 4(e)]. At $t = 5$ ms, the sound wave has not yet arrived at the corner ring and no significant difference can be found between the two cases [left panel of Fig. 4(d)]. By contrast, after the sound reaches the corner (e.g., $t = 15$ ms), the intensity is concentrated around the corner for $B \neq 0$, whereas, for $B = 0$, the intensity distributed over the edge sites [left panel of Fig. 4(d)]. These observations clearly demonstrate the emergence of acoustic second-order NHSE by a synthetic magnetic field.

IV. CONCLUSIONS

To sum up, we have explored the intricate physics and experimentally demonstrated the suppression or the creation of NHSE by SMFs. Our results demonstrate the rich potential in the creative control of waves by SMF in non-Hermitian systems. The boundary-localized skin modes can give rise to the unidirectional wave propagation, energy localization and enhanced absorption and emission. The introduction of a synthetic magnetic field plays a crucial role in the NHSE. The magnetic field breaks the time-reversal symmetry, leading to the creation of chiral edge states. Furthermore, the direction and strength of the synthetic magnetic field can influence the localization pattern of the skin modes, enabling the fine-tuning of the system's behavior. This sensitivity of the NHSE to the synthetic magnetic field, combined with the non-Hermitian characteristics, allows for the creation of reconfigurable topological devices. Such reconfigurable devices can adapt their functionality in response to external stimuli, such as strain[56] or other control parameters, which show great potential in a wide range of applications, from signal processing and wave manipulation to energy harvesting and active control systems. The interaction mechanisms of SMFs and NHSE reported here can be universally adapted for higher dimensional systems and other wave systems where effective magnetic fields can emerge, such as Dirac point systems with pseudomagnetic fields[54] and optical systems under time modulation[55]. The proposed coupled ring lattice is quite flexible to acquire various forms of SMFs and non-Hermiticity, and thus provides a versatile platform to study the diverse interplay between magnetic fields and non-Hermitian phenomena in both acoustics and photonics[57].

SUPPLEMENTARY MATERIAL

See the supplementary material for details on the calculations of the tight-binding model and coupled ring resonator model, eigenenergy profiles under different magnetic fields, measured time evolution of acoustic pressure signals, calculated intensity field for the finite lattice without SMF and more experimental results for the finite 2D lattice, experimental realizations of the on-site non-Hermiticity, discussion on the complex spectrum, changing the localization positions of the skin corner localization and suppression and creation of NHSE in one single lattice.

ACKNOWLEDGMENTS

G.M. acknowledges support from the National Key R&D Program of China 2022YFA1404400 and Hong Kong Research Grants Council (12301822 and RFS2223-2S01). H.G. and Z.S. acknowledge support from the Research Grants Council of Hong Kong SAR (15214323, 15200922 and 15202820). H.X. acknowledges support from the start-up fund of The Chinese University of Hong Kong.

DATA AVAILABILITY

The data that support the findings of this study are available from the corresponding author upon reasonable request.

REFERENCES

[1] L. Feng, R. El-Ganainy, and L. Ge, "Non-Hermitian photonics based on parity–time symmetry," Nat. Photon. **11**, 752–762 (2017).
[2] R. El-Ganainy, K. G. Makris, M. Khajavikhan, Z. H. Musslimani, S. Rotter, and D. N. Christodoulides, "Non-Hermitian physics and PT symmetry," Nat. Phys. **14**, 11–19 (2018).
[3] M.-A. Miri and A. Alù, "Exceptional points in optics and photonics," Science **363**, eaar7709 (2019).
[4] E. J. Bergholtz, J. C. Budich, and F. K. Kunst, "Exceptional topology of non-Hermitian systems," Rev. Mod. Phys. **93**, 015005 (2021).
[5] K. Ding, C. Fang, and G. Ma, "Non-Hermitian topology and exceptional-point geometries," Nat. Rev. Phys. **4**, 745–760 (2022).
[6] R. Lin, T. Tai, L. Li, and C. H. Lee, "Topological non-Hermitian skin effect," Front. Phys. **18**, 53605 (2023).
[7] V. M. Alvarez, J. B. Vargas, and L. F. Torres, "Non-Hermitian robust edge states in one dimension: Anomalous localization and eigenspace condensation at exceptional points," Phys. Rev. B **97**, 121401 (2018).
[8] Y. Xiong, "Why does bulk boundary correspondence fail in some non-Hermitian topological models," J. Phys. Commun. **2**, 035043 (2018).
[9] Z. Gong, Y. Ashida, K. Kawabata, K. Takasan, S. Higashikawa, and M. Ueda, "Topological phases of non-Hermitian systems," Phys. Rev. X **8**, 031079 (2018).
[10] S. Yao and Z. Wang, "Edge states and topological invariants of non-Hermitian systems," Phys. Rev. Lett. **121**, 086803 (2018).
[11] F. K. Kunst, E. Edvardsson, J. C. Budich, and E. J. Bergholtz, "Biorthogonal bulk-boundary correspondence in non-Hermitian systems," Phys. Rev. Lett. **121**, 026808 (2018).
[12] C. H. Lee and R. Thomale, "Anatomy of skin modes and topology in non-Hermitian systems," Phys. Rev. B **99**, 201103 (2019).
[13] N. Okuma, K. Kawabata, K. Shiozaki, and M. Sato, "Topological origin of non-Hermitian skin effects," Phys. Rev. Lett. **124**, 086801 (2020).
[14] K. Zhang, Z. Yang, and C. Fang, "Correspondence between winding numbers and skin modes in non-Hermitian systems," Phys. Rev. Lett. **125**, 126402 (2020).
[15] D. S. Borgnia, A. J. Kruchkov, and R.-J. Slager, "Non-Hermitian boundary modes and topology," Phys. Rev. Lett. **124**, 056802 (2020).
[16] S. Weidemann, M. Kremer, T. Helbig, T. Hofmann, A. Stegmaier, M. Greiter, R. Thomale, and A. Szameit, "Topological funneling of light," Science **368**, 311–314 (2020).
[17] Q. Lin, T. Li, L. Xiao, K. Wang, W. Yi, and P. Xue, "Observation of non-Hermitian topological Anderson insulator in quantum dynamics," Nat. Commun. **13**, 3229 (2022).
[18] L. Zhang, Y. Yang, Y. Ge, Y.-J. Guan, Q. Chen, Q. Yan, F. Chen, R. Xi, Y. Li, D. Jia, *et al.*, "Acoustic non-hermitian skin effect from twisted winding topology," Nat. Commun. **12**, 6297 (2021).

[19] H. Gao, H. Xue, Z. Gu, L. Li, W. Zhu, Z. Su, J. Zhu, B. Zhang, and Y. Chong, "Anomalous Floquet non-Hermitian skin effect in a ring resonator lattice," Phys. Rev. B **106**, 134112 (2022).

[20] X. Zhang, Y. Tian, J.-H. Jiang, M.-H. Lu, and Y.-F. Chen, "Observation of higher-order non-hermitian skin effect," Nat. Commun. **12**, 5377 (2021).

[21] Z. Gu, H. Gao, H. Xue, J. Li, Z. Su, and J. Zhu, "Transient non-hermitian skin effect," Nat. Commun. **13**, 7668 (2022).

[22] T. Wan, K. Zhang, J. Li, Z. Yang, and Z. Yang, "Observation of the geometry-dependent skin effect and dynamical degeneracy splitting," Sci. Bull. **68**, 2330–2335 (2023).

[23] Q. Zhou, J. Wu, Z. Pu, J. Lu, X. Huang, W. Deng, M. Ke, and Z. Liu, "Observation of geometry-dependent skin effect in non-hermitian phononic crystals with exceptional points," Nat. Commun. **14**, 4569 (2023).

[24] M. Brandenbourger, X. Locsin, E. Lerner, and C. Coulais, "Non-reciprocal robotic metamaterials," Nat. Commun. **10**, 4608 (2019).

[25] A. Ghatak, M. Brandenbourger, J. Van Wezel, and C. Coulais, "Observation of non-hermitian topology and its bulk–edge correspondence in an active mechanical metamaterial," Proc. Natl. Acad. Sci. U.S.A. **117**, 29561–29568 (2020).

[26] W. Wang, X. Wang, and G. Ma, "Non-Hermitian morphing of topological modes," Nature **608**, 50–55 (2022).

[27] W. Wang, M. Hu, X. Wang, G. Ma, and K. Ding, "Experimental realization of geometry-dependent skin effect in a reciprocal two-dimensional lattice," Phys. Rev. Lett. **131**, 207201 (2023).

[28] K. Wang, A. Dutt, K. Y. Yang, C. C. Wojcik, J. Vučković, and S. Fan, "Generating arbitrary topological windings of a non-Hermitian band," Science **371**, 1240–1245 (2021).

[29] Y. G. Liu, Y. Wei, O. Hemmatyar, G. G. Pyrialakos, P. S. Jung, D. N. Christodoulides, and M. Khajavikhan, "Complex skin modes in non-Hermitian coupled laser arrays," Light Sci. Appl. **11**, 336 (2022).

[30] S. Liu, R. Shao, S. Ma, L. Zhang, O. You, H. Wu, Y. J. Xiang, T. J. Cui, and S. Zhang, "Non-hermitian skin effect in a non-hermitian electrical circuit," Research (2021), 10.34133/2021/5608038.

[31] D. Zou, T. Chen, W. He, J. Bao, C. H. Lee, H. Sun, and X. Zhang, "Observation of hybrid higher-order skin-topological effect in non-hermitian topolectrical circuits," Nat. Commun. **12**, 7201 (2021).

[32] H. Zhang, T. Chen, L. Li, C. H. Lee, and X. Zhang, "Electrical circuit realization of topological switching for the non-hermitian skin effect," Physical Review B **107**, 085426 (2023).

[33] S. Longhi, "Non-Hermitian gauged topological laser arrays," Ann. Phys. **530**, 1800023 (2018).

[34] B. Zhu, Q. Wang, D. Leykam, H. Xue, Q. J. Wang, and Y. Chong, "Anomalous single-mode lasing induced by nonlinearity and the non-Hermitian skin effect," Phys. Rev. Lett. **129**, 013903 (2022).

[35] A. McDonald and A. A. Clerk, "Exponentially-enhanced quantum sensing with non-hermitian lattice dynamics," Nat. Commun. **11**, 5382 (2020).

[36] J. C. Budich and E. J. Bergholtz, "Non-hermitian topological sensors," Phys. Rev. Lett. **125**, 180403 (2020).

[37] H. Yuan, W. Zhang, Z. Zhou, W. Wang, N. Pan, Y. Feng, H. Sun, and X. Zhang, "Non-hermitian topolectrical circuit sensor with high sensitivity," Adv. Sci. , 2301128 (2023).

[38] L. Landau, "Diamagnetismus der metalle," Z. Phys. **64**, 629–637 (1930).

[39] G. Liang and Y. Chong, "Optical resonator analog of a two-dimensional topological insulator," Phys. Rev. Lett. **110**, 203904 (2013).

[40] M. Lu, X.-X. Zhang, and M. Franz, "Magnetic suppression of non-hermitian skin effects," Phys. Rev. Lett. **127**, 256402 (2021).

[41] K. Shao, Z.-T. Cai, H. Geng, W. Chen, and D. Xing, "Cyclotron quantization and mirror-time transition on nonreciprocal lattices," Phys. Rev. B **106**, L081402 (2022).

[42] Q. Lin, W. Yi, and P. Xue, "Manipulating directional flow in a two-dimensional photonic quantum walk under a synthetic magnetic field," Nat. Commun. **14**, 6283 (2023).

[43] H. T. Teo, S. Mandal, Y. Long, H. Xue, and B. Zhang, "Pseudomagnetic suppression of non-Hermitian skin effect," arXiv:2307.05099 (2023).

[44] C.-A. Li, B. Trauzettel, T. Neupert, and S.-B. Zhang, "Enhancement of second-order non-Hermitian skin effect by magnetic fields," Phys. Rev. Lett. **131**, 116601 (2023).

[45] X. Wen, C. Qiu, Y. Qi, L. Ye, M. Ke, F. Zhang, and Z. Liu, "Acoustic landau quantization and quantum-hall-like edge states," Nat. Phys. **15**, 352–356 (2019).

[46] D. De Bernardis, Z.-P. Cian, I. Carusotto, M. Hafezi, and P. Rabl, "Light-matter interactions in synthetic magnetic fields: Landau-photon polaritons," Phys. Rev. Lett. **126**, 103603 (2021).

[47] See Supplementary Material for more details.

[48] H. Li, A. Mekawy, A. Krasnok, and A. Alù, "Virtual parity-time symmetry," Phys. Rev. Lett. **124**, 193901 (2020).

[49] F. Guan, X. Guo, K. Zeng, S. Zhang, Z. Nie, S. Ma, Q. Dai, J. Pendry, X. Zhang, and S. Zhang, "Overcoming losses in superlenses with synthetic waves of complex frequency," Science **381**, 766–771 (2023).

[50] S. Kim, Y.-G. Peng, S. Yves, and A. Alù, "Loss compensation and super-resolution in metamaterials with excitations at complex frequencies," Phys. Rev. X **13**, 041024 (2023).

[51] S. Mittal, V. V. Orre, G. Zhu, M. A. Gorlach, A. Poddubny, and M. Hafezi, "Photonic quadrupole topological phases," Nat. Photonics **13**, 692–696 (2019).

[52] M. Hafezi, S. Mittal, J. Fan, A. Migdall, and J. Taylor, "Imaging topological edge states in silicon photonics," Nat. Photonics **7**, 1001–1005 (2013).

[53] M. Hafezi, E. A. Demler, M. D. Lukin, and J. M. Taylor, "Robust optical delay lines with topological protection," Nat. Phys. **7**, 907–912 (2011).

[54] M. Yan, W. Deng, X. Huang, Y. Wu, Y. Yang, J. Lu, F. Li, and Z. Liu, "Pseudomagnetic fields enabled manipulation of on-chip elastic waves," Phys. Rev. Lett. **127**, 136401 (2021).

[55] S. Mittal, G. Moille, K. Srinivasan, Y. K. Chembo, and M. Hafezi, "Topological frequency combs and nested temporal solitons," Nat. Phys. **17**, 1169–1176 (2021).

[56] N. Levy, S. Burke, K. Meaker, M. Panlasigui, A. Zettl, F. Guinea, A. C. Neto, and M. F. Crommie, "Strain-induced pseudo–magnetic fields greater than 300 tesla in graphene nanobubbles," Science **329**, 544–547 (2010).

[57] Z. Gao, X. Qiao, M. Pan, S. Wu, J. Yim, K. Chen, B. Midya, L. Ge, and L. Feng, "Two-dimensional reconfigurable non-hermitian gauged laser array," Phys. Rev. Lett. **130**, 263801 (2023).